Supplementary information

Self-powered TENG Sensor Based on Hybrid Energy: Tilt Angle and Wind Speed -Research on Dual Parameter sensing and Intelligent Fault Warning of Transmission Lines

Changxin Liu [a, *] Guangchao Qiao [a], Chen Chen [a], Yong Cui [b], Zhenqing Liu [b], Yang Liu [b], Dazhi Zhang [a], Mingyu Lu [a,*], Nan Liu [c, *]

[a]*College of Marine Engineering, Dalian Maritime University, Dalian Liaoning 116026, China*

[b]*Delin Land Port Supply Chain Services Co., Ltd, Anshan Liaoning 114010, China*

[c]*Dalian Medical University, Dalian Liaoning 116044, China*

Section S1: Output performance of WG-TENG at ambient temperatures from -10°C to 50°C.

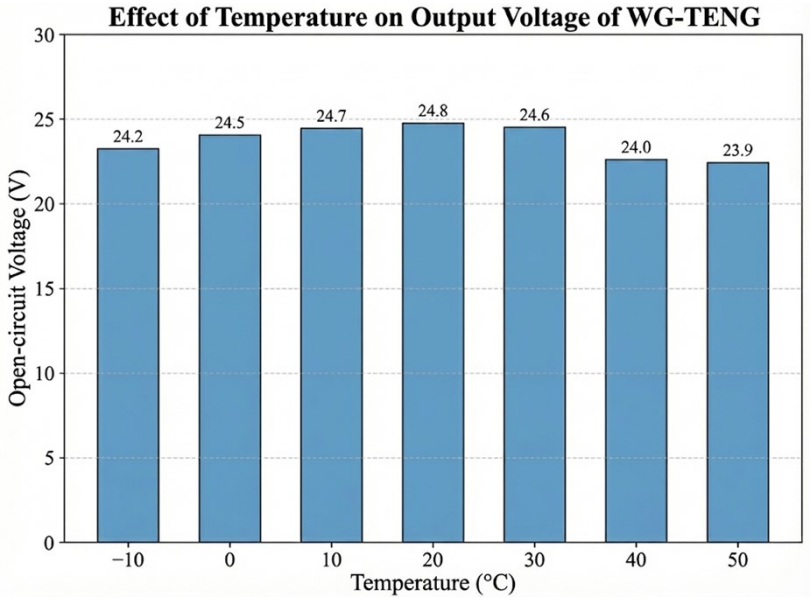

Figure S1. Output performance of WG-TENG at ambient temperatures from -10°C to 50°C

As illustrated in Figure S1, to assess the environmental adaptability of the WG-TENG for outdoor transmission line monitoring, this study experimentally investigated the output performance of the WG-TENG under varying ambient temperatures ranging from -10°C to 50°C. During the tests, the wind speed and tilt angle were fixed at 10 m/s and 60°, respectively, with a relative humidity of

approximately 40%, while other variables were controlled to minimize interference. The experimental results indicate that the open-circuit voltage demonstrated a relatively stable trend across the tested temperature range. The WG-TENG achieved a peak output of 24.8 V at 20°C. Although a slight attenuation in voltage was observed as the temperature increased, the device maintained over 96% of its maximum output, confirming its operational stability over a wide temperature range. This minor decline can be primarily attributed to the accelerated thermal decay of triboelectric charges on the PTFE surface at elevated temperatures. Overall, these findings substantiate that the proposed WG-TENG exhibits sufficient thermal stability to function reliably under typical transmission line operating conditions.

Section S2: Output performance of WG-TENG at relative humidity levels from 30% to 90%.

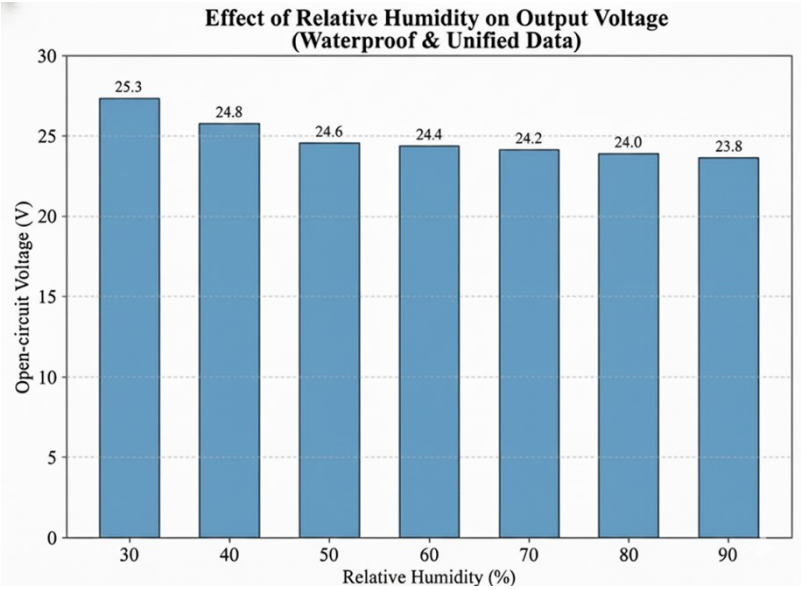

Figure S2. Output performance of WG-TENG at relative humidity levels from 30% to 90%

Reliability under high-humidity conditions represents a significant challenge for conventional TENG devices. Consequently, this study systematically evaluated the output voltage characteristics of the WG-TENG across relative humidity (%RH) levels ranging from 30% to 90%. As depicted in Figure S2, the device demonstrated commendable stability against moisture ingress. Under controlled test conditions with a fixed temperature of 20°C, a wind speed of 10 m/s, and a tilt angle of 60°, the output voltage of the WG-TENG remained stable throughout the entire humidity range. Specifically, the open-circuit voltage exhibited only a slight decrease from 25.3 V (at 30% RH) to 23.8 V (at 90% RH).

This corresponds to a voltage retention rate exceeding 95%, which stands in stark contrast to conventional TENGs that typically suffer from severe charge dissipation in highly humid environments. This result effectively validates the reliability of the proposed device for operation in high-humidity outdoor settings.

Section S3: Output current waveform of WG-TENG across a wide humidity range of 30%RH to 90%RH.

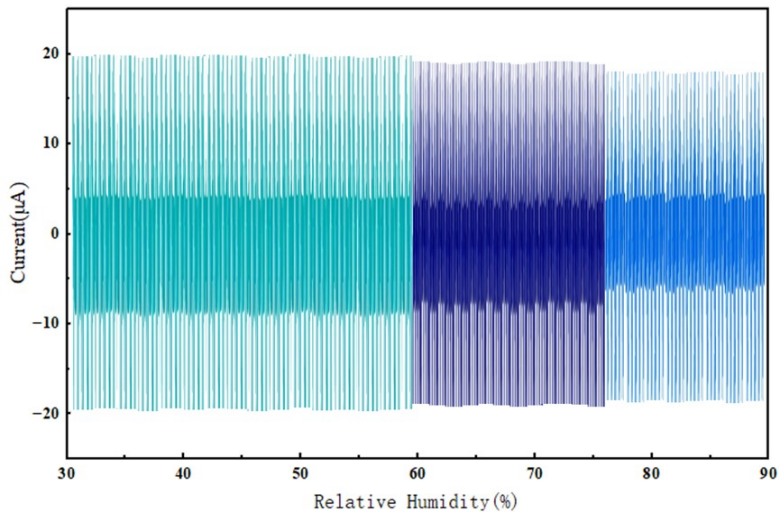

Figure S3. Output current waveform of WG-TENG across a wide humidity range of 30%RH to 90%RH

Under experimental conditions with a fixed tilt angle of 30° and a wind speed of 8 m/s, this study systematically investigated the influence pattern of humidity on the current output of the device. As shown in Figure S3, as the relative humidity gradually increased from 30%RH to 90%RH, the current waveform exhibited characteristic three-stage variations. Within the 30%RH–60%RH range, the maximum amplitude of the current waveform was regular, with the peak value stabilizing between 19–20 μA and a fluctuation coefficient of only ±0.5 μA. This indicates that within this humidity range, the micro/nano-structures on the surface of the triboelectric layer effectively suppressed water vapor adsorption, the charge density remained stable, and the charge transfer at the triboelectric interface was sufficient and regular. Within the 60%RH–80%RH range, the current amplitude showed a slight decreasing trend. This is attributed to the formation of a discontinuous thin water film on the PTFE surface by water vapor, which acts as a weak conductive pathway, leading to partial leakage of surface charges and a decrease in charge transfer efficiency. Within the high-humidity range of 80%RH–90%RH, the current experienced a slight attenuation. The periodic characteristics of the overall waveform

were significantly weakened, accompanied by low-amplitude clutter interference. This occurs because, at this stage, a continuous conductive water film forms on the surface of the triboelectric layer, charge leakage intensifies, and the charge transfer process at the triboelectric interface is severely inhibited. These experimental results demonstrate that the WG-TENG possesses excellent output stability within the 30%RH–60%RH range, which is common outdoors, and can maintain effective signal output in environments with humidity below 80%RH. This provides experimental support for its long-term service in the complex humidity environments encountered by outdoor transmission lines.

Section S4: Classification ROC curves for WG-TENG sensing signals across different wind speed intervals.

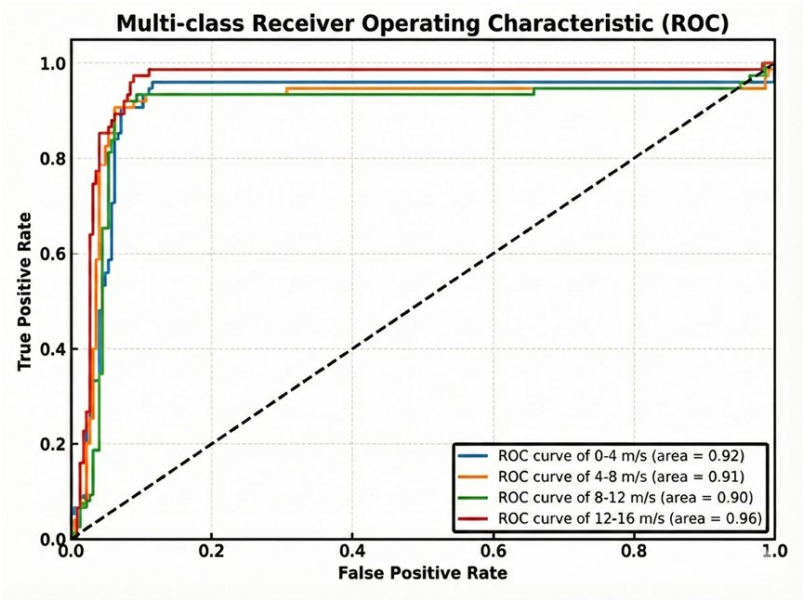

Figure S4. Classification ROC curves for WG-TENG sensing signals across different wind speed intervals

Figure S4 presents the performance evaluation of the wind speed interval classification model based on the output signals from the WG-TENG. This figure utilizes Receiver Operating Characteristic (ROC) curves and the Area Under the Curve (AUC) to quantify the model's classification capability. The experiments were conducted under fixed conditions: a tilt angle of 30° and a relative humidity of 50%RH. The common outdoor wind speed range for transmission lines (0–16 m/s) was divided into four key intervals for classification validation. The primary objective is to assess the recognition accuracy of the signal identification method for different

wind speed signals. In this figure, the False Positive Rate (FPR) represents the probability of the model incorrectly classifying non-target wind speed intervals as the target interval, while the True Positive Rate (TPR) denotes the probability of correctly identifying the target wind speed interval. The dashed diagonal line serves as the benchmark for random classification (AUC = 0.5). A ROC curve that deviates further from this line, accompanied by an AUC value closer to 1, indicates superior classification performance. As evident from the characteristics of the curves, the classification models for all four wind speed intervals demonstrate excellent recognition capability. The 12–16 m/s high wind speed interval achieved the highest AUC value, indicating that the model possesses optimal recognition accuracy for strong wind signals that are likely to induce conductor galloping. Although the AUC value for the 8–12 m/s interval is slightly lower, it still resides within the excellent classification threshold above 0.9. This minor decrease is primarily due to the partial overlap in signal characteristics between this interval and its adjacent ones, which slightly increases the difficulty of differentiation. The core value of this result lies in validating the compatibility of WG-TENG sensing signals with conventional classification methods. By extracting time-domain and frequency-domain features of the triboelectric signals, the model can stably distinguish between different wind speed intervals. Furthermore, the AUC values for all intervals significantly exceed the excellent classification threshold of 0.9, far outperforming the random classification benchmark. Considering the operational and maintenance requirements of transmission lines, different wind speed intervals correspond to varying safety risks. For instance, high wind speeds can easily trigger conductor galloping, while medium and low wind speeds require stability monitoring. The high classification accuracy of this model ensures unbiased identification of wind speed levels, providing reliable signal pre-processing support for subsequent fault early warning. Simultaneously, the stable performance of the model across the entire wind speed range confirms the high distinguishability of WG-TENG sensing signals. This result is consistent with the core design logic of the dual-parameter self-powered TENG sensing method proposed in the main paper. It also provides an experimental foundation for the precise application of WG-TENG in the complex wind speed environments encountered by transmission lines.

Section S5: t-SNE Visualization Analysis of Model Feature Learning Capability.

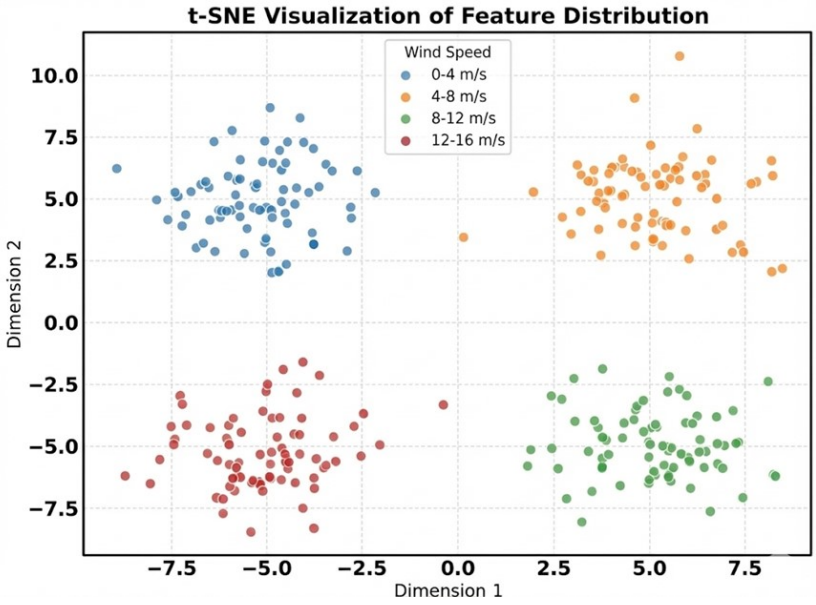

Figure S5. t-SNE Visualization Analysis of Model Feature Learning Capability

To further investigate the internal feature extraction mechanism and discrimination capability of the 1D-CNN model, this study employed the t-distributed Stochastic Neighbor Embedding (t-SNE) algorithm to perform dimensionality reduction and visualization analysis on the high-dimensional feature vectors output from the model's fully connected layer. As illustrated in Figure S5, the deep feature distributions corresponding to different wind speed categories were extracted from the test set. In the figure, each data point represents an individual test sample, with distinct colors assigned to different wind speed categories. After processing by the 1D-CNN for feature extraction, samples from different categories formed well-separated and independent clusters in the two-dimensional space. This clustering phenomenon demonstrates the model's exceptional feature discrimination ability and strong resistance to interference. The results reveal that the original complex time-series electrical signals, after being transformed by the convolutional neural network, exhibit a pronounced clustering effect in the feature space. Data points representing different wind speed intervals automatically aggregate into clearly demarcated clusters, characterized by substantial inter-cluster distances and high intra-cluster compactness. This clear inter-class separation provides intuitive evidence that the network has successfully learned robust features capable of characterizing wind speed variations, rather than merely memorizing the training data. Consequently, these findings corroborate the high classification accuracy exhibited by the model, as

reflected in the confusion matrix analysis.

Section S6: Composition and Function of Signal Acquisition and Reception Units.

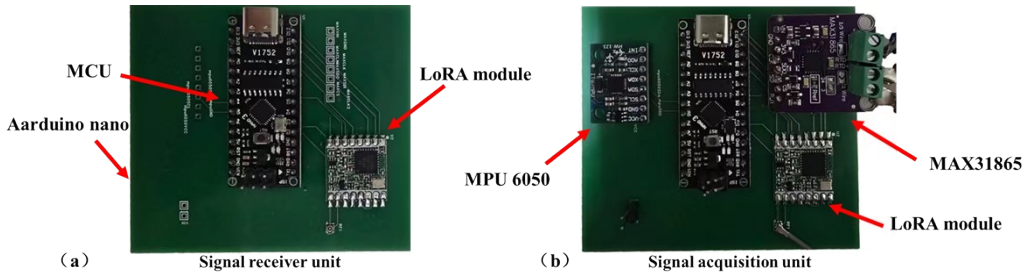

Figure S6. (a) Signal transmission unit; (b) Signal reception unit

Figure S6. (a) and (b) show the physical diagrams of the signal receiving unit and the signal acquisition (transmission) unit, respectively, which together constitute a complete monitoring node system.

The signal receiving unit (Figure a) also uses an Arduino Nano (MCU) as its core controller, paired with a LoRa module for data reception. Deployed at the operation and maintenance center or base station, it is responsible for receiving and parsing data from on-site monitoring points. The received data is synchronously imported into the database system, and the supporting early warning system automatically triggers an alert when the data exceeds preset thresholds. This realizes real-time monitoring and anomaly warning of transmission line conditions, thereby reducing the risk of failures and disasters.

The signal acquisition unit (Figure b) integrates modules for core control, data collection, and wireless transmission. It uses an Arduino Nano (MCU) as the main control unit, equipped with an MPU6050 accelerometer and a MAX31865 temperature transmitter for multi-parameter physical sensing, and employs a LoRa module for low-power wireless data transmission. The Arduino Nano is responsible for sampling and digitizing the analog/digital signals output by the sensors. Based on pre-calibrated sensitivity coefficients, it converts voltage signals into actual physical quantities such as inclination, vibration, and temperature. The processed data is then packaged according to the communication protocol and transmitted to the receiving end via the LoRa module.

Section S7: Output performance of WG-TENG at dust

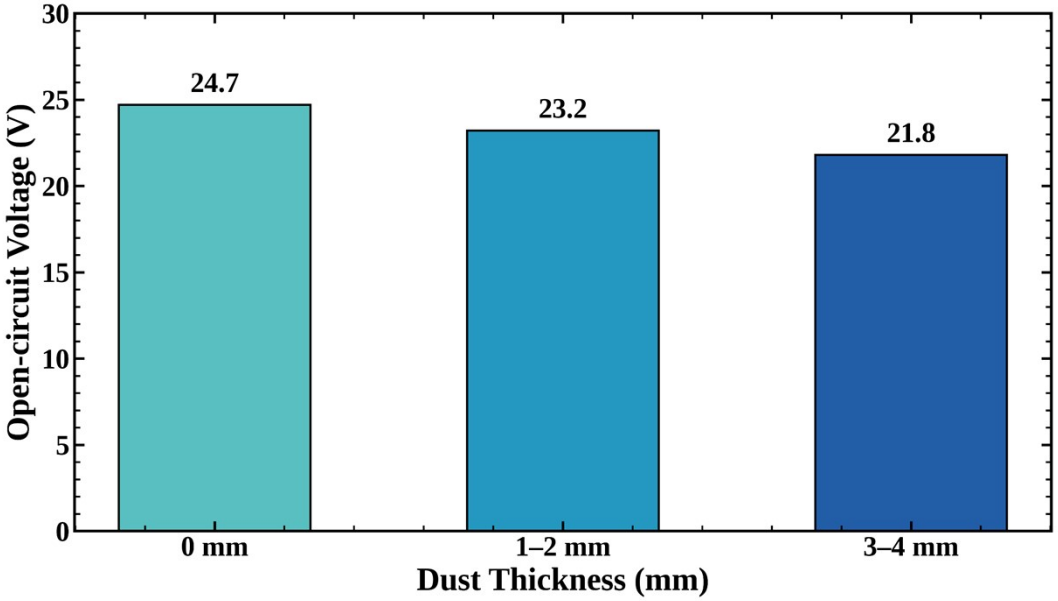

Figure S7 Output performance of WG-TENG at dust

To further verify the robustness and adaptability of the system in real complex outdoor environments, this study supplemented output performance tests of the WG-TENG under different dust accumulation thicknesses. During the experiments, we simulated actual dust accumulation conditions on transmission lines, artificially controlling the dust thickness on the experimental platform. Steady-state tests were conducted under three typical gradients: 0 mm (clean baseline), 1-2 mm (slight dust), and 3-4 mm (moderate dust), and the open-circuit voltage output characteristics of the device were recorded.

As shown in the figure S7, the WG-TENG delivers an open-circuit voltage of 24.7 V under clean conditions. When covered with 1-2 mm of slight dust, the output voltage only slightly decreases to 23.2 V. Even under moderate dust accumulation of 3-4 mm, the device still maintains an output voltage of 21.8 V. The overall values show only minor fluctuations and all remain above 20 V.

This phenomenon clearly indicates that a small amount of dust deposition does not substantially damage the core triboelectric and electrostatic induction mechanisms of the WG-TENG, and the device can still maintain efficient and stable electrical output and sensing performance. These experiments fully demonstrate that the system

possesses excellent environmental tolerance and structural stability under typical outdoor dust interference. It can effectively guarantee the continuity and reliability of data acquisition for transmission line online monitoring, providing strong experimental support for dealing with complex and non-ideal real-world working conditions.

Section S8: Theoretical model and experimental data validation

Regarding the issue that the WG-TENG theoretical model (Equations 1-7) established in Section 2.3 lacked experimental validation and fitting metrics, we have supplemented systematic quantitative verification in the revised manuscript. Specifically, we performed nonlinear least-squares fitting on the theoretical model in three dimensions: voltage–tilt angle (V-θ), current–wind speed (I-v), and current–tilt angle (I-θ), and fully provided the fitting equations, goodness-of-fit R^2, and error analysis. The relevant results are shown in Figure S8. The detailed discussion is as follows.

Validation of the voltage-tilt angle relationship:

Nonlinear least-squares fitting was performed on the experimental data for the $V \propto \sin\theta$ relationship predicted by Equation (7). As shown in Figure S8(a), the fitting equation is $V = 37.18 \sin\theta + 1.19$ (V) with a goodness-of-fit $R^2 = 0.9952$; the light shaded area represents the 95% confidence band, indicating that the theoretical model has high explanatory power for the experimental data.

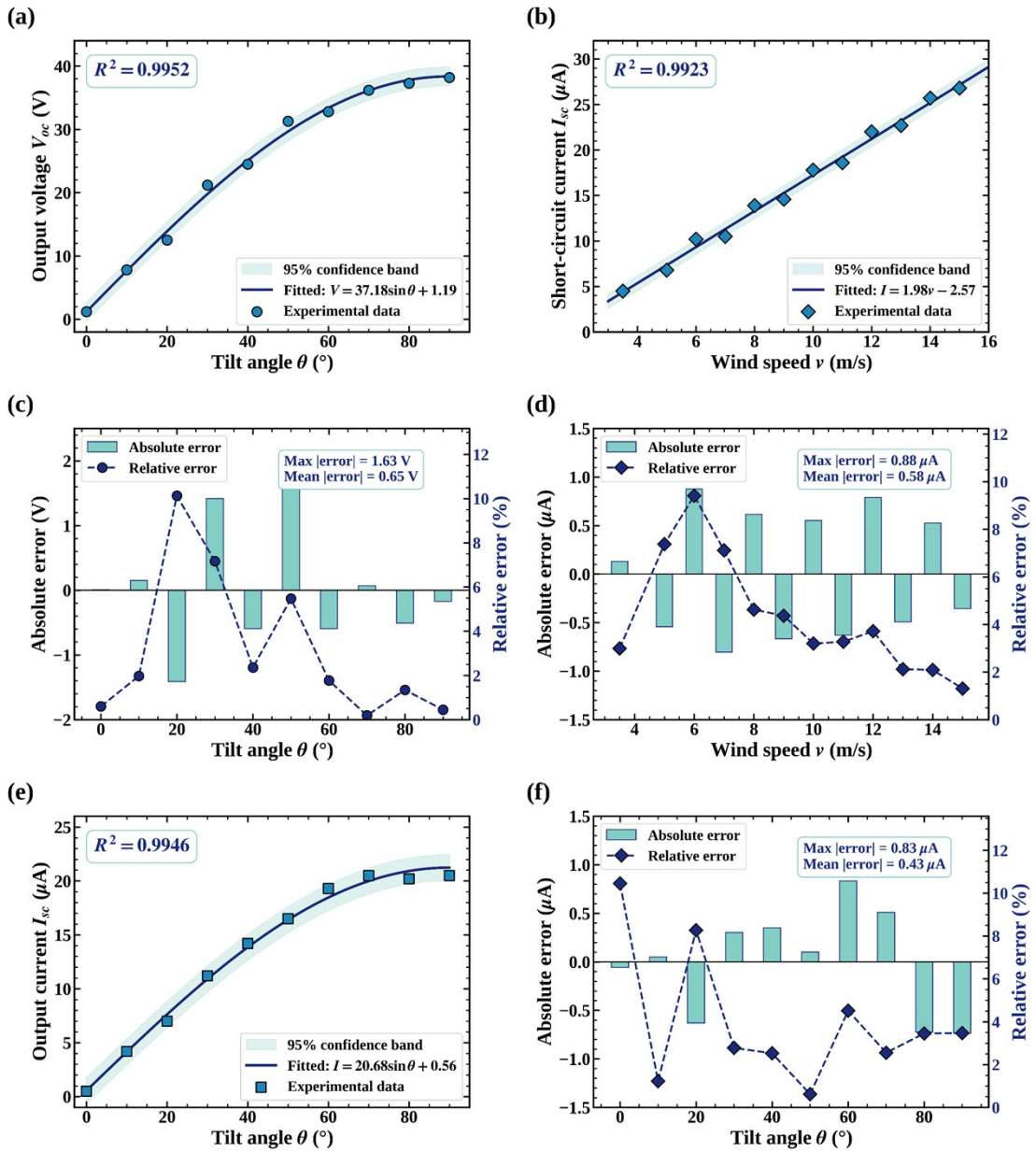

Figure S8 Three-dimensional experimental fitting verification of the WG-TENG theoretical model. (a) Fitting curve of V–θ; (b) Fitting curve of I–v; (c) Absolute and relative error distributions of V–θ; (d) Absolute and relative error distributions of I–v; (e) Fitting curve of I–θ; (f) Absolute and relative error distributions of I–θ.

The corresponding error analysis is shown in Figure S8(c): the maximum absolute error is 1.63 V, the mean absolute error is 0.65 V, the maximum relative error is 10.13% (appearing in the low-angle region near 20°), and the mean relative error is 3.15%. The relatively large deviation in the low-angle region mainly arises from the preload and nonlinear characteristics of the compression spring. At small tilt

angles, the adjustment of the contact area is more sensitive to assembly tolerances, causing the charge transfer to deviate from the ideal assumption. In contrast, in the medium and high-angle regions, the spring compression enters the linear working range, and the fitting accuracy is significantly improved. In addition, a baseline offset of approximately 1.2 V exists at 0°, which originates from the residual contact caused by the spring preload; this effect is not included in the assumptions of the theoretical model.

Validation of the current-wind speed relationship:

For the linear relationship $I \propto v$ predicted by Equation (5), the fitting result is shown in Figure S8(b). The equation is $I=1.98v-2.57$ (μA) with R^2 =0.9923. The fitted sensitivity of 1.98 μA/(m/s) agrees well with the theoretical value of 2 μA/(m/s), with a relative deviation of only 1%. The corresponding error analysis is shown in Figure 2(d): the maximum absolute error is 0.88 μA, the mean absolute error is 0.58 μA, the maximum relative error is 9.41%, and the mean relative error is 4.30%. The deviation is mainly concentrated in the low wind speed range (3-7 m/s), consistent with the observation in Figure S8(d) of the main text: transient effects during fan start-stop dynamics and flow field establishment lead to large fluctuations at low wind speeds. In the high wind speed region, the fitting accuracy is significantly improved after the flow field becomes stable.

Validation of the current-tilt angle relationship:

To further fully verify the relationship of I with θ predicted by Equation (5), the supplementary fitting result is shown in Figure S8(e). The equation is $I=20.68\sin\theta+0.56$ (μA) with R^2 =0.9946. The constant term 0.56 μA originates from the baseline current caused by residual contact due to spring preload, consistent with the baseline offset mechanism in the path. The error analysis is shown in Figure S8(f): the maximum absolute error is 0.83 μA, the mean absolute error is 0.43 μA, and the mean relative error is 3.99%.

The above analysis demonstrates excellent agreement between the established WG-TENG theoretical model and the experimental results: the R^2 values of the three fittings are 0.9952, 0.9923, and 0.9946, all above 0.99, and the average relative errors

are all controlled within 5%. The residual deviations mainly arise from the simplifications adopted in the theoretical model, including idealizing the spring behavior as linear, neglecting bearing friction losses, and assuming constant contact pressure. The fitting results fully validate the effectiveness and reliability of the established theoretical model within the accuracy requirements for engineering applications. The above supplementary validations and relevant data have been added to the revised manuscript and supporting information. We sincerely appreciate the reviewer's valuable comments.

Section S9: Parameter Optimization of Interdigital Electrodes

In this study, systematic optimization experiments were supplemented for three key structural parameters of the interdigital electrode, namely the number of electrode pairs, electrode width, and electrode spacing. The experiments were carried out under constant conditions of a tilt angle of 90° and a wind speed of 15 m/s. The control variable method was adopted to measure the open-circuit voltage and short-circuit current of the WG-TENG under different structural parameters, and the results are presented in Figure S9.

The influence of the number of electrode pairs n on the output performance is shown in Figure 5(a). As the number of electrode pairs *n* increases from 4 to 10, both the output voltage and current show a significant upward trend; when n exceeds 10, the output performance begins to decline. This phenomenon can be explained by Equation (4). On the one hand, increasing the number of electrode pairs raises the number of electrode cycles passed by the rotating PTFE film per unit time, improving the output frequency and accumulated charge quantity. On the other hand, an excessive number of electrode pairs inevitably reduces the width of a single electrode within the limited annular perimeter, which intensifies the edge effect and decreases the effective charge transfer amount in a single contact-separation cycle. The competitive relationship between the two effects determines the optimal number of electrode pairs. The experimental results indicate that the output reaches the

maximum at n=10, with Voc =38.2V and Isc =20.0μA, which is regarded as the optimal configuration.

The influence of electrode width w on output performance is illustrated in Figure 5(b). As the electrode width w increases from 1 mm to 4 mm, the output voltage and current continuously rise; when the width further increases to 5-7 mm, the output decreases instead. This is because an increase in the width of a single electrode directly enlarges the contact area per cycle, which effectively improves the charge transfer amount in a single cycle according to Equation (4). However, an excessively large electrode width limits the number of electrode pairs that can be arranged within a fixed circumference and reduces the cyclic frequency of rotational sweeping. The experimental results confirm that w=4mm is the optimal electrode width, corresponding to Voc =38.2V and Isc =20.0μA. The effect of electrode spacing d on output performance is presented in Figure 5(c). The output increases significantly as the spacing d rises from 0.5 mm to 2.0 mm, and gradually declines when d further increases to 3.5 mm. The underlying physical mechanism is as follows: when the electrode spacing is too small, charges between adjacent electrodes are prone to crosstalk through the fringe electric field, resulting in partial charge cancellation and reduced output amplitude. A moderate increase in spacing can effectively suppress crosstalk and allow the two sets of electrodes to complete independent charging and discharging processes. Nevertheless, an excessively large spacing markedly reduces the proportion of effective electrode area, thereby lowering the overall output. At the optimal spacing of d=2.0mm, both Voc =38.2V and Isc =20.0μA reach their peak values. Based on the above three groups of optimization experiments, the final structural parameters of the interdigital electrode adopted in this work are determined as follows: number of electrode pairs n=10, electrode width w=4mm, and electrode spacing d=2.0mm. Under the same experimental conditions, this set of parameters enables the WG-TENG to achieve the maximum voltage and current output, providing a reliable structural basis for all subsequent performance tests in this paper.

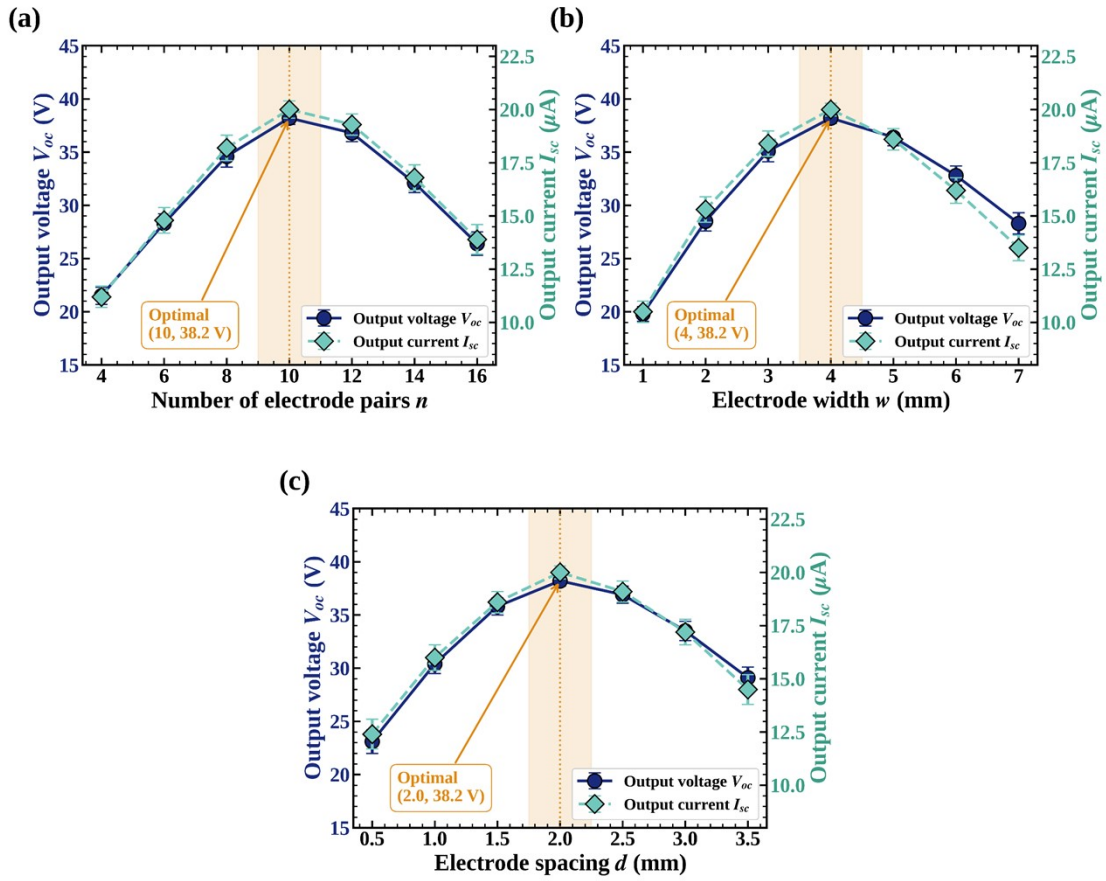

Figure S9 Optimization experiment of key structural parameters of forked electrode (a) The influence of electrode pairs n; (b) The influence of electrode width w; (c) The influence of electrode spacing d